

Orientation and size dependence of the elastic properties of zinc oxide nanobelts

A J Kulkarni¹, M Zhou^{1,3} and F J Ke²

¹ The George W Woodruff School of Mechanical Engineering, Georgia Institute of Technology, Atlanta, GA 30332-0405, USA

² Department of Physics, Beijing University of Aeronautics and Astronautics, Beijing 100083, People's Republic of China

E-mail: min.zhou@me.gatech.edu

Received 11 July 2005, in final form 30 August 2005

Published 11 October 2005

Online at stacks.iop.org/Nano/16/2749

Abstract

Molecular dynamics simulations are performed to characterize the response of zinc oxide (ZnO) nanobelts to tensile loading. The ultimate tensile strength (UTS) and Young's modulus are obtained as functions of size and growth orientation. Nanobelts in three growth orientations are generated by assembling the unit wurtzite cell along the [0001], [01 $\bar{1}$ 0], and [2 $\bar{1}$ $\bar{1}$ 0] crystalline axes. Following the geometric construction, dynamic relaxation is carried out to yield free-standing nanobelts at 300 K. Two distinct configurations are observed in the [0001] and [01 $\bar{1}$ 0] orientations. When the lateral dimensions are above 10 Å, nanobelts with rectangular cross-sections are seen. Below this critical size, tubular structures involving two concentric shells similar to double-walled carbon nanotubes are obtained. Quasi-static deformations of belts with [2 $\bar{1}$ $\bar{1}$ 0] and [01 $\bar{1}$ 0] orientations consist of three stages, including initial elastic stretching, wurtzite-ZnO to graphitic-ZnO structural transformation, and cleavage fracture. On the other hand, [0001] belts do not undergo any structural transformation and fail through cleavage along (0001) planes. Calculations show that the UTS and Young's modulus of the belts are size dependent and are higher than the corresponding values for bulk ZnO. Specifically, as the lateral dimensions increase from 10 to 40 Å, decreases between 38–76% and 24–63% are observed for the UTS and Young's modulus, respectively. This effect is attributed to the size-dependent compressive stress induced by tensile surface stress in the nanobelts. [01 $\bar{1}$ 0] and [2 $\bar{1}$ $\bar{1}$ 0] nanobelts with multi-walled tubular structures are seen to have higher values of elastic moduli (~340 GPa) and UTS (~36 GPa) compared to their wurtzite counterparts, echoing a similar trend in multi-walled carbon nanotubes.

(Some figures in this article are in colour only in the electronic version)

1. Introduction

As nanotechnology progresses and complex nanosystems are fabricated, a rising impetus is being given to the development of multi-functional and size-dependent materials. The term size dependence refers to the emergence of exciting properties as dimensions approach microns and nanometres. Nanomaterials, due to their high surface-to-

volume ratios as compared with bulk materials, exhibit unique structures and properties. Zinc oxide (ZnO) is one such versatile material that has been explored for applications in sensing, environmental monitoring, bio-medical systems and communications technology. It has emerged as an important component for integration in nanoelectromechanical systems (NEMS) because (i) it is a semiconductor, (ii) it is piezoelectric (owing to its non-centrosymmetric structure), and (iii) it is bio-safe and bio-compatible [1]. Recently, ZnO nanostructures

³ Author to whom any correspondence should be addressed.

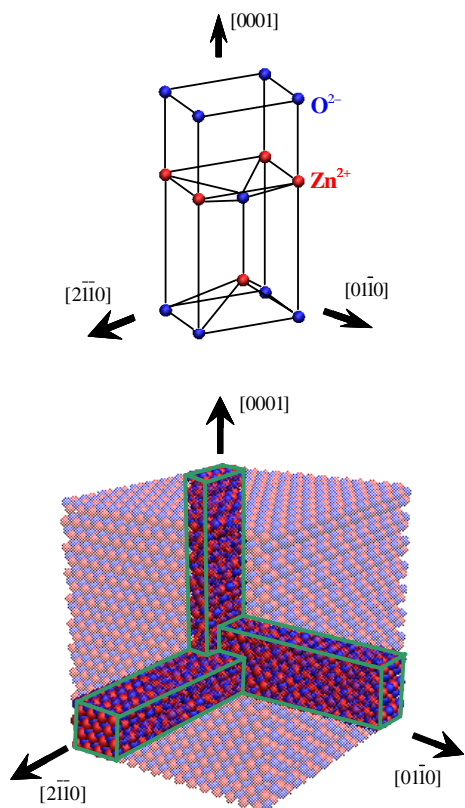


Figure 1. Unit wurtzite cell and assembled nanobelts.

with rectangular cross-sections, referred to as nanobelts, have been grown through vapour deposition [2]. The synthesis is based on thermal evaporation of ZnO powders in a tube furnace and condensation of the vapours on an alumina plate. The most common growth directions for the nanobelts are along the [0001] and [01 $\bar{1}$ 0] crystalline axes of the wurtzite structure. Growth along the [2 $\bar{1}$ $\bar{1}$ 0] orientation is resisted by the energy barrier due to surface polarization, but such structures have also been reported [3]. The nanobelts have found applications in ultra-sensitive sensors for detecting chemical and biological species, nanoresonators, nanocantilevers, and field effect transistors [4–7]. ZnO nanostructures can also serve as building blocks for other nanosystems.

The integration of these nanostructures in any system entails detailed understanding of their inherent properties, functionalities and behaviour. Application-based property evaluation of the components is a basic requirement for the design of systems. Responses to stimuli such as applied stress and thermal gradients as well as size and temperature effects on behaviour have to be characterized. Structural transformations specific to the nanoscale and their reversibility have to be studied in order to unleash the potential of these nanostructures. Experimental evaluations of such properties at the nanoscale are challenging or even infeasible. Atomistic simulations provide an alternative means for analysing the properties of materials. Molecular dynamics (MD) simulations are increasingly being used to study the mechanical behaviour of nanostructures [8–16]. The deformations analysed involve both quasi-static and dynamic (with strain rates up to 10^9 s $^{-1}$)

Table 1. Nanobelt dimensions along the three principal growth orientations (Å).

Growth along	Dimension along		
	[0001]	[01 $\bar{1}$ 0]	[2 $\bar{1}$ $\bar{1}$ 0]
[0001]	151.82	18.95	18.95
[01 $\bar{1}$ 0]	20.63	105.52	20.73
[2 $\bar{1}$ $\bar{1}$ 0]	21.12	21.22	102.85

conditions. The higher strain rates were often necessary to reach required strain levels with available computer resources. In the present work, MD simulations of deformation under quasi-static tensile loading are carried out. The ultimate tensile strength (UTS), strain at failure and Young's modulus are evaluated. Strain-induced structural transformations are characterized. The orientation and size dependence of the mechanical response is also analysed. The differences between behaviours at the nanoscale and in bulk are highlighted.

2. Computational framework

The as-synthesized nanobelts are single crystalline, wurtzite-structured with lattice constants $a = 3.249$ Å and $c = 5.206$ Å. Their thickness is between 5 and 20 nm with typical width-to-thickness ratios of 5–10 [2]. The computational models are generated by repeating the wurtzite cell along the three growth directions, as shown in figure 1. The minimum cross-sectional size analysed is determined based on the cutoff radii in the interatomic potential employed. Specifically, the size is chosen such that the short-range cutoff distance is smaller than the smallest belt dimension and long-range interactions are properly considered. The nanobelts analysed have a length of 150 Å. To study the size effect, four cross-sectional sizes (10 × 10, 20 × 20, 30 × 30 and 40 × 40 Å) are considered; see table 1.

A Buckingham-type interatomic potential of the form

$$E(r_{ij}) = \frac{q_i q_j}{r_{ij}} + A \exp\left(\frac{-r_{ij}}{\rho}\right) - \frac{C}{r_{ij}^6} \quad (1)$$

implemented in the MD code⁴ DLPOLY 2.14 is used. Here, r_{ij} is the distance between two ions, q_i is the charge on ion i and A , ρ and C are potential parameters. The first term in equation (1) considers the long-range Coulomb interactions due to electric charges and the second and third terms model short-range interactions. Anion–anion interactions include both the long-range and short-range terms. Anion–cation interactions are modelled using the Born–Mayer form which neglects the last (attractive) term. Cation–cation interactions involve only the long-range charge effect. Calculation of the long-range Coulomb force is carried out using the Ewald sum which is computationally efficient and unconditionally convergent. The periodicity required for the Ewald sum is introduced using a supercell concept, in which the simulation box is defined considerably larger than the nanobelt. A favourable comparison in the energy prediction from the Ewald sum and direct Coulomb sum is observed in the simulations (figure 2).

⁴ DLPOLY is a molecular simulation routine written by W Smith and T R Forester, copyright of CCLRC for the Central Laboratory of Research Councils, Daresbury Laboratory at Daresbury, near Warrington (1996).

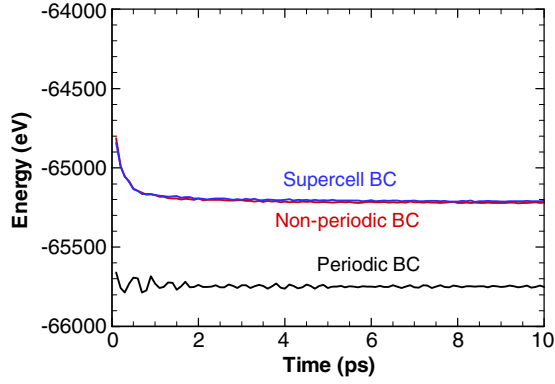


Figure 2. Comparison of energy levels from supercell, no-periodic, and periodic boundary conditions.

Table 2. Short-range interaction parameters for zinc oxide.

Species		A (eV)	ρ (Å)	C (eV Å)
O^{2-}	O^{2-}	9547.96	0.219 16	32.0
Zn^{2+}	O^{2-}	529.70	0.3581	0.0
Zn^{2+}	Zn^{2+}	0.0	0.0	0.0

The parameters A , ρ and C of the potential are fitted to the structure and properties of ZnO using classical and quantum mechanical methods [17]. These parameters are listed in table 2. The potential has been shown to accurately predict the equilibrium lattice energy, cell parameters, elastic and dielectric constants. Extensive perfect lattice, defect and monovalent ion incorporation simulations have been successfully carried out using this potential [17–19]. The potential also effectively predicts surface properties such as surface energies [17]. This is especially important in the simulations for nanobelts whose high surface-to-volume ratios are known to significantly affect behaviour. It should be noted that the empirical nature and the simplicity of the potential inherently include approximations which are justified only when the properties studied are satisfactorily predicted. Since only mechanical properties in the elastic regime are being explored here, the potential is used to analyse conditions for which it is developed and therefore is expected to work effectively [20]. *Ab initio* simulations could possibly enhance the accuracy of the results, but are impractical for the system sizes analysed here.

After geometric construction, the nanobelts are first equilibrated at 300 K for 10 ps with traction-free boundary conditions. Approximation to quasi-static tensile loading in each deformation increment is achieved in two steps. First, a velocity of 1 \AA ps^{-1} (ramped from 0) is applied to boundary atoms to effect the extension up to a displacement of $\sim 0.6 \text{ \AA}$. This is followed by equilibration of the entire structure for 3 ps with boundary atoms fixed at their current positions; see figure 3. This results in a nominal strain of 0.36% per deformation increment. The virial formula as modified by Zhou [21] in the form of

$$\sigma^{\alpha\beta} = \frac{1}{2\Omega} \left\{ \sum_i \sum_{j \neq i} f_{ij}^{\alpha} r_{ij}^{\beta} \right\} \quad (2)$$

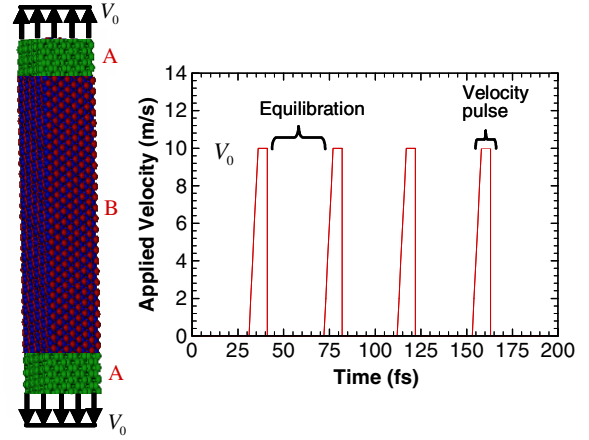


Figure 3. Quasi-static loading scheme consisting of the applied velocity pulse and the intermediate equilibration steps. The velocity boundary condition is applied to the boundary atoms (sections A). Section B is the actual specimen.

is used to calculate the stress. Here, Ω is the system volume, f_{ij} is the interparticle force between particles i and j , and r_{ij} is the separation distance between the two particles. The Young's modulus is obtained from the slope of the linear portion of the stress–strain curve.

3. Results and discussion

Equilibration and the subsequent tensile loading of the nanostructures result in orientation and size-specific behaviours.

3.1. Initial relaxation and surface reconstructions

The computationally generated nanobelts are dynamically relaxed to obtain their free-standing states at 300 K for 10 ps with traction-free boundary conditions. During equilibration, minimization of energy occurs through surface reconstruction and adjustment to the lattice spacing in the core. The surface reconstruction results from charge transfer and imbalance of ionic forces. For belts with larger cross-sections (lateral dimensions $> 2 \text{ nm}$), the surface-to-volume ratio is smaller and bulk energy constitutes a major portion of the total configurational energy. Consequently, surface reconstruction manifests itself in the form of decreased interlayer spacing between outer surface layers. As the belt size decreases, the surface-to-volume ratio increases and a larger portion of the atoms reside on the surface rather than in the interior. Figure 4 shows the increase in surface atoms (from 10 to 45%) as the lateral dimension is decreased from 50 to 10 Å. In smaller nanobelts, the natural tendency is to minimize the surface energy by extensive structural transformation.

The competition between core optimization and surface energy minimization results in two distinct configurations after equilibration. When lateral dimensions are above 10 Å, nanobelts with rectangular cross-sections are observed. The relaxation results in reconstruction only in the outer layers of (01 $\bar{1}$ 0) and (0001) surfaces. Figure 5 shows the inward movement of (0001) and (01 $\bar{1}$ 0) surface atoms. The trend is to reduce the interlayer spacing. (2 $\bar{1}$ $\bar{1}$ 0) surfaces do not show any

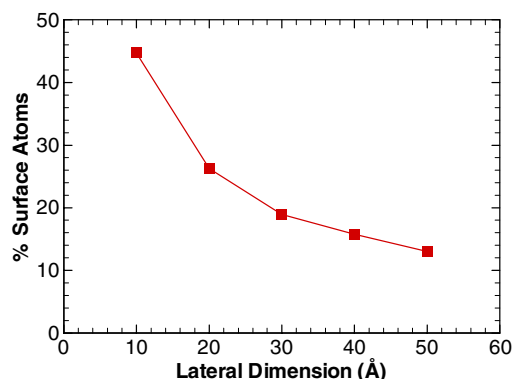


Figure 4. Fraction of surface atoms as a function of lateral dimensions of the nanobelt.

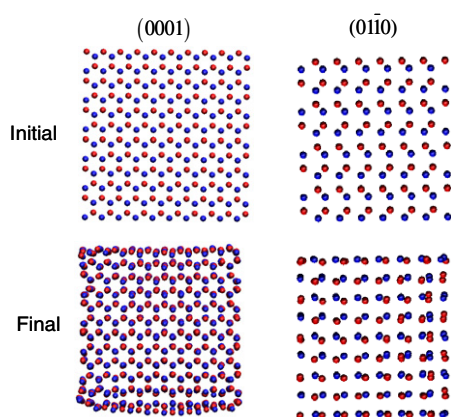


Figure 5. Surface configurations during equilibration. Reconstructions of the (0001) and (0110) surfaces are observed. The (2110) surface does not reconstruct.

reconstruction. It can be seen from the figure that the effect of surface reconstruction is limited to the two outer layers only while the interior maintains near bulk lattice positions. This observation is confirmed by a comparison of the radial distribution function (RDF) profiles for bulk ZnO and the nanobelt (see figure 6). The first and second peaks for both structures coincide, indicating that the core of the nanobelt retains the bulk wurtzite structure. To state it differently, the effect of surface reconstruction does not penetrate into the core. Similar reconstructions on (1010) and (0001) planes have been observed through low-energy electron diffraction [22].

Below the critical size of 10 Å, tubular structures involving two concentric shells similar to those of double-walled carbon nanotubes are observed in [0001] and [0110] belts (figure 7). Equilibration of [2110] nanobelts does not result in shell structure formation. The tubular structures have low-energy (0001) lateral surfaces, indicating a transformation driven by surface energy minimization [23]. Since belts with lateral dimensions smaller than 10 Å have ~45% of their atoms on surfaces, the contribution of surfaces to the total configurational energy in such cases is particularly high. As a result, structural change occurs over the entire belt, yielding the shell structures. Similar multi-shell and core-shell structures have been reported for metals [13, 24–26] and other layered inorganic materials such as W_s_2 , MoS_2 and $NiCl_2$ [27–29].

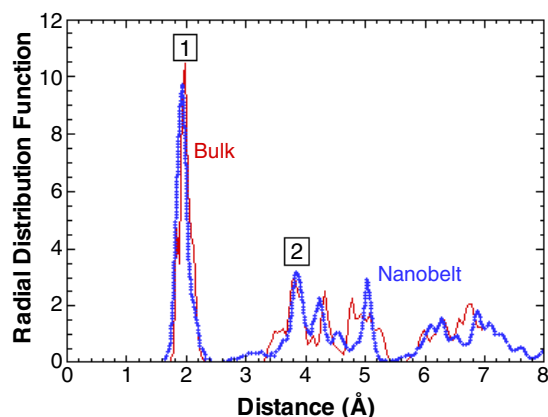


Figure 6. Comparison of the first and second neighbour peaks in the RDF for bulk and nanobelt structures.

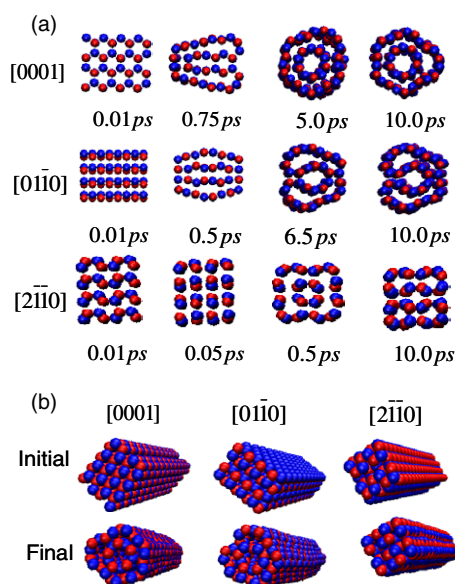


Figure 7. (a) Stages in the formation of the shell structures in [0001] and [0110] nanobelts. The [2110] belts show surface reconstruction without shell structure formation. (b) Initial and final views of nanobelts in the three growth orientations. All nanobelts shown have 10 Å × 10 Å cross-sections.

3.2. Orientation dependence of elastic response

Nanobelts with different growth orientations show distinct deformation behaviours under loading. The orientation dependence of elastic properties is analysed using belts 20 Å in lateral dimensions. Belts with cross-sectional dimensions smaller than 10 Å do not retain their initial wurtzite structure and their behaviour cannot be categorized according to crystalline orientations. The deformation of [2110] belts proceeds in three stages: initial elastic stretching, structural transformation from wurtzite-ZnO to graphitic-ZnO, and eventual shear failure, as shown in figure 8. Specifically, the stress–strain relation is essentially linear in the elastic regime. Deformation beyond the elastic regime results in a stress drop from 14.2 to 12 GPa. Such a softening behaviour is indicative of the initiation of martensitic transformation [30–36]. Similar martensitic transformations

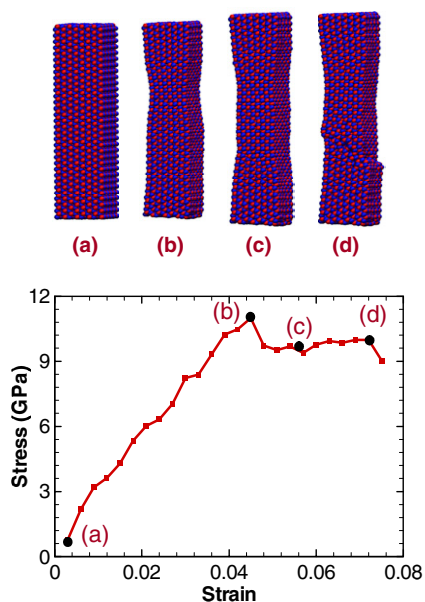


Figure 8. Tensile stress–strain curves for a $[2\bar{1}\bar{1}0]$ nanobelt. (a) Initial equilibrated stage, (b) initiation of structure transformation, (c) completion of the transformation over the entire specimen, and (d) failure by shear along $(\bar{1}2\bar{1}0)$ -type planes.

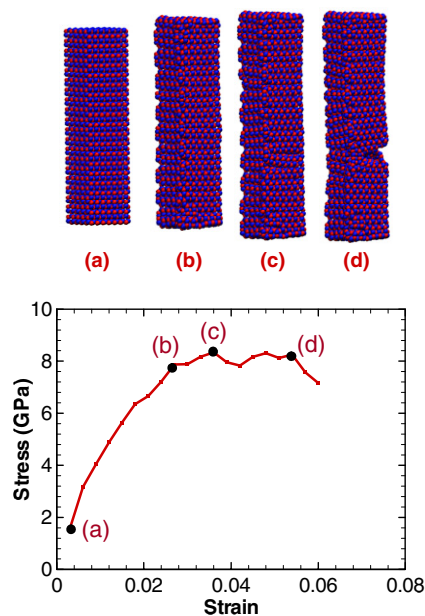


Figure 10. Tensile stress–strain response for a $[0001]$ nanobelt. (a) Initial equilibrated stage, (b) initiation of failure, (c) separation along (0001) -type planes, and (d) perfect cleavage on the (0001) planes.

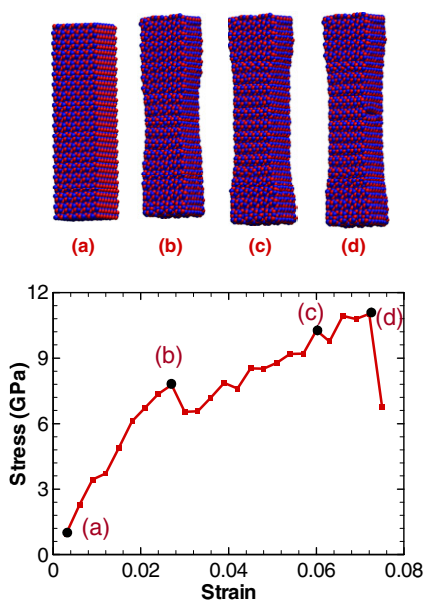


Figure 9. Tensile stress–strain curve for a $[01\bar{1}0]$ nanobelts. (a) Initial equilibrated state, (b) initiation of structure transformation, (c) completion of the transformation over the entire specimen, and (d) failure by shear along $(\bar{1}2\bar{1}0)$ -type planes.

have been reported in inorganic, non-metallic materials, the most notable being a wurtzite-to-graphite transformation in boron nitride [34]. The transformation results in a metastable hexagonal ($a = 3.57 \text{ \AA}$, $c = 4.2986 \text{ \AA}$) phase with its c -axis rotated by 90° relative to the initial structure (figure 11). As the deformation progresses, the transformed region sweeps through the whole specimen, without obvious increase in applied stress. Failure occurs at a strain of 7.2% through shear along $(\bar{1}2\bar{1}0)$ -type planes.

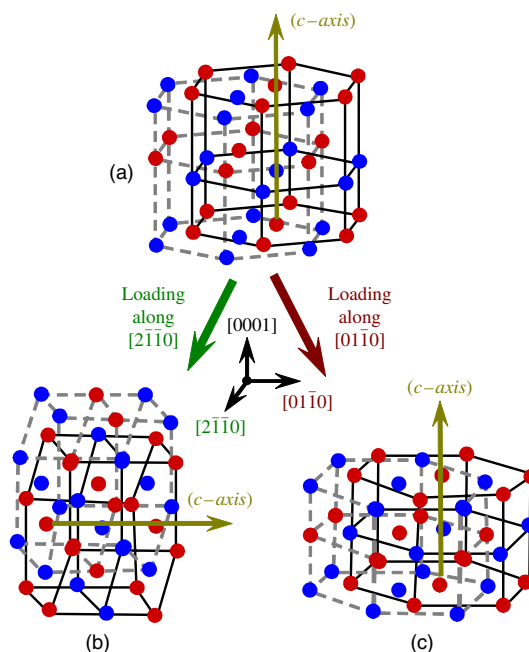


Figure 11. Nature of the structural transformation. (a) Initial wurtzite structure, (b) final rotated hexagonal phase for $[2\bar{1}\bar{1}0]$ nanobelts and (c) final hexagonal phase for $[01\bar{1}0]$ nanobelts.

Figure 9 shows the stress–strain curve of a $[01\bar{1}0]$ nanobelt with a lateral dimension of 20 \AA . Following initial elastic stretching, a structural transformation similar to that in the $[2\bar{1}\bar{1}0]$ nanobelt is observed. The difference here is that the c -axes of the original and resultant structures coincide (figure 11). This transformation begins at a strain of 2.7% and a stress level of 10.5 GPa. Failure occurs at a strain of 7.2% and a stress of 15 GPa. The lower strain at the nucleation of the

Table 3. Young's modulus for nanobelts of different orientations and size $20 \text{ \AA} \times 20 \text{ \AA}$ along with the corresponding values for the bulk structure.

Orientation	Young's modulus (GPa)	
	Nanobelt	Bulk
[0001]	172.65	119.7
[01 $\bar{1}$ 0]	254.19	156.2
[2 $\bar{1}$ $\bar{1}$ 0]	256.5	156.2

Table 4. Variations of the Young's modulus and UTS with lateral dimension.

Lateral dimension (\AA)	Young's modulus (GPa)			Ultimate tensile strength (GPa)		
	[2 $\bar{1}$ $\bar{1}$ 0]	[01 $\bar{1}$ 0]	[0001]	[2 $\bar{1}$ $\bar{1}$ 0]	[01 $\bar{1}$ 0]	[0001]
10	307.4	325.75	339.76	15.0198	23.38	36.332
20	256.5	254.19	172.65	13.76	12.689	10.922
30	210.31	219.89	140.37	9.1837	9.5246	8.6245

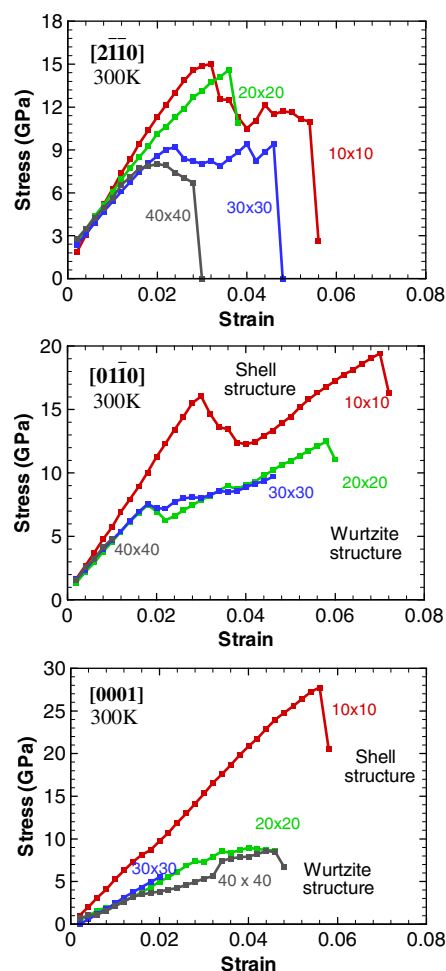
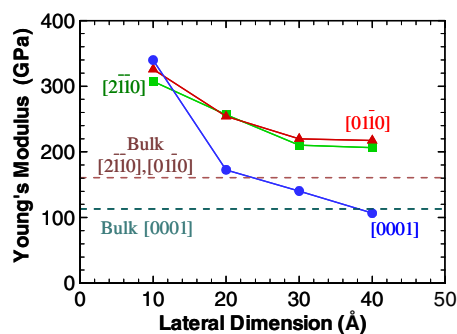
transformation and the increasing stress during transformation make the response of the [01 $\bar{1}$ 0] belt different from that of the [2 $\bar{1}$ $\bar{1}$ 0] belt. This belt fails through cleavage along ($\bar{1}2\bar{1}$ 0)-type planes.

The response of the [0001] belts resembles the bulk behaviour of ZnO. The stress–strain relation suggests a rather brittle response (figure 10) without phase transformation, consisting of elastic deformation cleavage fracture along (0001) planes. The failure strain is 5.4%.

The calculated elastic modulus values for the three orientations and the corresponding bulk values [37, 38] are summarized in table 3. The wurtzite structure is quasi-isotropic transversely with properties in the [01 $\bar{1}$ 0] and [2 $\bar{1}$ $\bar{1}$ 0] directions of the basal plane being similar to each other and different from those along the *c*-axis. This is indeed the case in the Young's modulus values and the UTS values obtained. However, there is a difference in the transformation strain and stress level for the two basal plane directions. In addition, [0001] nanobelts have a lower Young's modulus compared with belts of the other two orientations.

3.3. Size dependence of elastic response

The effect of specimen size on deformation is also analysed. Figure 12 shows the responses of belts of different sizes in all three directions. For each orientation, the Young's modulus and the UTS decreases as the size is increased. Their values are higher than the corresponding bulk values. Specifically, as the lateral dimensions increase from 10 to 40 \AA , decreases of 38%, 59%, 76% in UTS and 24, 33, 63% in Young's modulus are observed for the [2 $\bar{1}$ $\bar{1}$ 0], [01 $\bar{1}$ 0] and [0001] orientations respectively, as shown in table 4. Figures 13 and 14 show the variations of the Young's modulus and the UTS with belt size. A sudden drop is seen in both as the size increases from 10 to 20 \AA . The origin of this change is the difference in structures obtained after equilibration. The mechanism will be explained later. It is expected that, as the lateral dimension is further increased, the Young's modulus and the UTS eventually approach their respective bulk values.

**Figure 12.** Stress–strain curves as a function of lateral dimension for nanobelts of all three growth orientations.**Figure 13.** Young's modulus for the three orientations as functions of lateral dimension along with the corresponding bulk values.

The above trend can be explained based on the state of stress in the nanobelts. Surface-stress-induced internal (compressive) stress has been shown to be inversely proportional to the lateral dimension of the nanobelts [15, 39–41], effectively causing the size effect observed. When the cross-sectional dimensions are sufficiently large, the surface-stress-induced compressive stress is very small and the surface effects are inconsequential. As a result, the material behaviour approaches that at the bulk level.

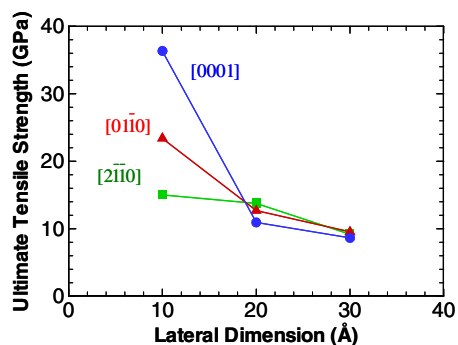


Figure 14. Ultimate tensile strengths for the three orientations as functions of lateral dimension.

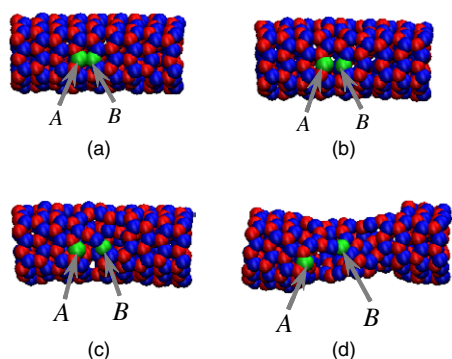


Figure 15. Failure mechanism in shell-structured nanobelts. (a) Initial configuration, (b), (c) separation of the atoms, and (d) subsequent shearing of the neighbouring atoms. Atoms (A, B) involved in local tensile bond failure are coloured green.

The deformation behaviours of $[01\bar{1}0]$ and $[0001]$ belts with lateral dimensions smaller than 10 \AA differ considerably from that of larger belts. This is attributed to the structural difference they have. The tubular structure offers a higher resistance to deformation as indicated by the high failure strength and Young's modulus values (59% and 76% higher, respectively, for the $[01\bar{1}0]$ and $[0001]$ orientations, over the values for a $40 \text{ \AA} \times 40 \text{ \AA}$ belt). This difference in strength and modulus is related to the difference in failure mechanisms between the rectangular and multi-shell belts. While the larger nanobelts fail by cleavage along certain crystallographic planes, the multi-shell belts fail due to local shear fracture [15]. Figure 15 illustrates the process of local bond failure followed by shearing in neighbouring atoms. This failure mechanism is responsible for the increased strength.

4. Conclusions

MD simulations of the tensile deformation of ZnO nanobelts are carried out to analyse their constitutive behaviour. The ultimate tensile strength and Young's modulus are calculated. Clear size and orientation effects on structures and properties are seen. Depending on the lateral dimensions, two distinct configurations (tubular and rectangular cross-sections) are observed. The critical radius for the structural transition is found to be 10 \AA . A similar size dependence is also observed in the elastic responses. Specifically, the Young's modulus and

UTS decrease significantly when the cross-sectional size of the nanobelts is increased. This behaviour is attributed to high compressive internal stress levels resulting from the surface stress and high surface-to-volume ratios at the nanoscale. The orientation dependence of the Young's modulus and the UTS is also characterized. It is found that the trend at the nanoscale follows that in bulk ZnO.

Acknowledgments

Support through the National Science Foundation through CAREER grant no. CMS9984298 and NASA Langley Research Center through grant number NAG-1-02054 is gratefully acknowledged. The work of FJK is supported by grant no. 10372012 of the Natural Science Foundation of China. Computations are carried out at the NAVO and ERDC MSRCs through AFOSR MURI number D49620-02-1-0382.

References

- [1] Wang Z L, Kong X Y, Ding Y, Gao P X, Hughes W L, Yang R and Zhang Y 2004 *Adv. Funct. Mater.* **14** 943–56
- [2] Pan Z W, Dai Z R and Wang Z L 2001 *Science* **291** 1947–9
- [3] Kong X Y and Wang Z L 2003 *Nano Lett.* **3** 1625–31
- [4] Arnold M S, Avouris P, Pan Z W and Wang Z L 2003 *J. Phys. Chem.* **107** 659–63
- [5] Bai X D, Gao P X, Wang Z L and Wang W G 2003 *Appl. Phys. Lett.* **82** 4806–8
- [6] Comini E, Faglia G, Sberveglieri G, Pan Z W and Wang Z L 2002 *Appl. Phys. Lett.* **81** 1869–71
- [7] Hughes W L and Wang Z L 2003 *Appl. Phys. Lett.* **82** 2886–8
- [8] Diao J, Gall K and Dunn M L 2004 *J. Mech. Phys. Solids* **52** 1935–62
- [9] Mehrez H, Ciraci S, Fong C Y and Erkoç S 1997 *J. Phys.: Condens. Matter* **9** 10843–54
- [10] Branicio P S and Rino J-P 2000 *Phys. Rev. B* **62** 16950–5
- [11] Komanduri R, Chandrasekaran N and Raff L M 2001 *Int. J. Mech. Sci.* **43** 2237–60
- [12] Komanduri R, Chandrasekaran N and Raff L M 2003 *Mater. Sci. Eng. A* **340** 58–67
- [13] Ju S-P, Lin J-S and Lee W-J 2004 *Nanotechnology* **15** 1221–5
- [14] Liang W and Zhou M 2003 Size and strain rate effects in tensile deformation of Cu nanowires *Nanotechnology Conf. and Trade Show* (San Francisco, CA: Computational Publications) pp 452–5
- [15] Gall K, Diao J and Dunn M L 2004 *Nano Lett.* **4** 2431–6
- [16] Diao J, Gall K and Dunn M L 2004 *Nano Lett.* **4** 1863–7
- [17] Binks D J 1994 Computational modelling of zinc oxide and related oxide ceramics *PhD* University of Surrey, Harwell
- [18] Binks D J and Grimes R W 1993 *J. Am. Ceram. Soc.* **76** 2370–2
- [19] Grimes R W, Binks D J and Lidiard A B 1995 *Phil. Mag. A* **72** 651–68
- [20] Grimes R W 2005 personal communication
- [21] Zhou M 2003 *Proc. R. Soc. A* **459** 2347–92
- [22] Duke C B, Lubinsky A R, Lee B W and Mark P 1976 *J. Vac. Sci. Technol.* **13** 761–8
- [23] Gulseren O, Ercolessi F and Tosatti E 1998 *Phys. Rev. Lett.* **80** 3775–8
- [24] Bilalbegovic G 1998 *Phys. Rev. B* **58** 15412–5
- [25] Bilalbegovic G 2000 *Comput. Mater. Sci.* **18** 333–8
- [26] Bilalbegovic G 2000 *Solid State Commun.* **115** 73–6
- [27] Hacothen Y R, Grunbaum E, Tenne R, Sloan J and Hutchison J L 1998 *Nature* **395** 336–7
- [28] Margulis L, Salitra G and Tenne R 1993 *Nature* **365** 113–4
- [29] Tenne R, Margulis L, Genut M and Hodes G 1992 *Nature* **360** 444–6
- [30] Olson G B and Cohen M 1982 Theory of martensitic nucleation: a current assessment *Proc. Int. Conf. on Solid-Solid Phase Transformations* ed H I Aaronson,

- R F Sekerka and C M Wayman (Pittsburgh, PA: AIME) pp 1145–64
- [31] Nakanishi N, Nagasawa A and Murakami Y 1982 *Proc. ICOMAT-82; J. Physique* **43** C4 35–55
- [32] Olson G B and Cohen M 1982 *Proc. ICOMAT-82; J. Physique Coll.* **43** C4 75–88
- [33] Mendelson S 1982 *Proc. ICOMAT-82; J. Physique* **43** C4 139–44
- [34] Kriven W M 1982 Shear transformations in inorganic materials *Proc. Int. Conf. Solid to Solid Phase Transformations* ed D E L H Aaronson, R F Sekerka and C M Wayman (Pittsburgh, PA: AIME) pp 1507–32
- [35] Geuenin G and Gobin P F 1982 *Proc. ICOMAT-82; J. Physique* **43** C4 57–63
- [36] Clapp P C and McLaughlin D 1980 *ICOMAT: Proc. Int. Conf. on Martensitic Transformations* pp 322–44
- [37] Lee W, Jeong M-C and Myoung J-M 2004 *Nanotechnology* **15** 254–9
- [38] Zaoui A and Sekkal W 2002 *Phys. Rev. B* **66** 174106-1–6
- [39] Liang W and Zhou M 2005 *J. Eng. Mater. Technol.* **127** 123–33
- [40] Sander S 2003 *Curr. Opin. Solid State Mater. Sci.* **7** 51–7
- [41] Diao J, Gall K and Dunn M L 2003 *Nat. Mater.* **2** 656–60